

## Introducing the MISR Level 2 Near Real-Time Aerosol Product

Marcin. L. Witek<sup>1</sup>, Michael J. Garay<sup>1</sup>, David J. Diner<sup>1</sup>, Michael A. Bull<sup>1</sup>, Felix C. Seidel<sup>1</sup>, Abigail M. Nاستان<sup>1</sup>, and Earl G. Hansen<sup>1</sup>

<sup>1</sup>Jet Propulsion Laboratory, California Institute of Technology, 4800 Oak Grove Drive, Pasadena, CA 91109, USA

Corresponding author: Marcin L. Witek, email: marcin.l.witek@jpl.nasa.gov

### **Abstract**

Atmospheric aerosols are an important element of Earth's climate system, and have significant impacts on the environment and on human health. Global aerosol modeling has been increasingly used for operational forecasting and as support to decision making. For example, aerosol analyses and forecasts are routinely used to provide air quality information and alerts in both civilian and military applications. The growing demand for operational aerosol forecasting calls for additional observational data that can be assimilated into models to improve model accuracy and predictive skill. These factors have motivated the development, testing, and release of a new near real-time (NRT) level 2 (L2) aerosol product from the Multi-angle Imaging SpectroRadiometer (MISR) instrument on NASA's Terra platform. The NRT product capitalizes on the unique attributes of the MISR aerosol retrieval approach and product contents, such as reliable aerosol optical depth as well as aerosol microphysical information. Several modifications are described that allow for rapid product generation within a three-hour window following acquisition of the satellite observations. Implications for the product quality and consistency are discussed as compared to the current operational L2 MISR aerosol product. Several ways of implementing additional use-specific retrieval screenings are also highlighted.

© 2021. California Institute of Technology. Government sponsorship acknowledged

## 31 **1. Introduction**

32

33 Atmospheric aerosols have for long been recognized to influence the climate, environment, and  
34 human health (e.g., IPCC, 2013; Lelieveld et al., 2015; Shindell et al., 2013; Turnock et al.,  
35 2020). They also affect satellite remote sensing of important geophysical parameters such as  
36 ocean color (e.g., Frouin et al., 2019; Gordon, 1997) or greenhouse gas abundance (Butz et al.,  
37 2009; Frankenberg et al., 2012; Houweling et al., 2005). Aerosol particles and their properties  
38 have been extensively studied in-situ and remotely: from the ground, in the air, and from space.  
39 These observational data vary in spatial and temporal coverage, but usually only offer  
40 snapshots of local conditions. Since atmospheric aerosols have a life cycle ranging from hours  
41 to days, numerical modeling of their emission, transport, and deposition has filled the coverage  
42 gaps and extended our understanding of their global impacts. This has given rise to a number of  
43 global aerosol reanalyses (Buchard et al., 2017; Gelaro et al., 2017; Inness et al., 2013, 2019;  
44 Lynch et al., 2016; Randles et al., 2017; Rienecker et al., 2011) that provide a long-range,  
45 gridded, and internally consistent outlook on aerosol burdens around the world. Furthermore,  
46 global aerosol modeling has been increasingly used for operational forecasting (e.g., Xian et al.,  
47 2019) and as support to decision making, for example in air quality alerts and in non-civilian  
48 applications (Liu et al., 2007).

49 The growing demand for consistent gridded aerosol products has been driving  
50 development and steady improvement of numerical predictions. For example, the International  
51 Cooperation for Aerosol Prediction initiative was founded in 2010 (Benedetti et al., 2011; Reid et  
52 al., 2011), with one of its goals being the development of global multi-model aerosol forecasting  
53 ensemble for basic research and operational use (Xian et al., 2019). Still, models suffer from  
54 often poorly resolved aerosol emissions and sinks and can be affected by errors in the  
55 underlying meteorology. As a result, systematic and sampling-related biases in aerosol fields  
56 are often found between model simulations and satellite observations (e.g., Buchard et al.,  
57 2015; Colarco et al., 2010; Lamarque et al., 2013; Zhang and Reid, 2009). An effective way to  
58 mitigate some of these problems is by assimilating aerosol observations into numerical models  
59 (e.g., Bocquet et al., 2015; Fu et al., 2017; Sekiyama et al., 2010; Di Tomaso et al., 2017;  
60 Werner et al., 2019; Zhang et al., 2008). Satellite observations of aerosol optical and  
61 microphysical properties are inseparable from these data assimilation activities as they offer the  
62 necessary data volume, near-global coverage, and frequent repeat cycle. However, an often-  
63 considerable latency for generating science-quality “standard” satellite products (8 to 40 hours)  
64 renders them unsuitable for operational forecasting. This has led to the development of aerosol

65 products within the time frame required by modeling centers, usually three hours from satellite  
66 overpass. A number of near real-time (NRT) products has emerged.

67 One example of a platform that provides users with NRT satellite products and imagery  
68 is NASA's Land, Atmosphere Near real-time Capability for EOS (LANCE) project  
69 (<https://earthdata.nasa.gov/earth-observation-data/near-real-time>). A range of instruments  
70 deliver various Level 1 (L1) and Level 2 (L2) data products  
71 ([https://earthdata.nasa.gov/collaborate/open-data-services-and-software/data-information-](https://earthdata.nasa.gov/collaborate/open-data-services-and-software/data-information-policy/data-levels)  
72 [policy/data-levels](https://earthdata.nasa.gov/collaborate/open-data-services-and-software/data-information-policy/data-levels)), including radiances, land surface properties, and atmospheric  
73 thermodynamics and composition within three hours from satellite observation. NRT aerosol  
74 products are currently available from the Moderate Resolution Imaging Spectroradiometer  
75 (MODIS), Ozone Monitoring Instrument (OMI), and Visible Infrared Imaging Radiometer Suite  
76 (VIIRS). NASA's Multi-angle Imaging SpectroRadiometer (MISR) currently provides NRT  
77 radiance and cloud motion vector products. The purpose of this paper is to introduce a new  
78 MISR NRT L2 aerosol product available within LANCE.

79 This paper is organized as follows. Section 2 and 3 provide brief descriptions of the  
80 MISR instrument and the data processing sequence, respectively. Section 4 first outlines the  
81 cloud identification methods employed in the MISR aerosol algorithm and then describes  
82 algorithmic modifications introduced in the NRT processing. Adjustments to cloud and retrieval  
83 screening parameters and their implications are discussed. The global distributions of the NRT  
84 product and comparisons of total and fractional AODs with the standard aerosol product are  
85 presented in Section 5. Section 6 provides a summary.

86

## 87 **2. MISR instrument and aerosol data product**

88

89 The MISR instrument flies aboard the NASA Earth Observing System (EOS) Terra satellite,  
90 launched in December 1999 to a sun-synchronous descending polar orbit, at an orbital altitude  
91 of 705 km, an orbital period of 99 minutes, and an equatorial crossing time of 10:30 a.m. local  
92 time. MISR makes 14.56 orbits per day with a repetition cycle (revisit) of 16 days. The orbit  
93 tracks are georeferenced to a fixed set of 233 ground paths. With a cross-track swath of about  
94 380 km, total Earth coverage is obtained every 9 days at the equator and every 2 days at high  
95 latitudes.

96 MISR contains nine pushbroom cameras with viewing angles at the Earth's surface  
97 ranging from 0° (nadir) to +/- 70.5° oriented along the direction of the flight track. A point on the  
98 ground is imaged by all nine cameras in approximately 7 minutes. The cameras make

99 observations of reflected solar radiance in four spectral bands, centered at 446 (blue), 558  
100 (green), 672 (red), and 866 (near-infrared) nm. The spatial resolution depends on the camera  
101 and wavelength. The red band has a full 275 m resolution in all cameras. The other three  
102 spectral channels are averaged onboard to a 1.1 km resolution in global-mode operation (Diner  
103 et al., 1998), with the exception of the nadir camera which preserves the full 275 m resolution in  
104 all spectral channels. See <https://misr.jpl.nasa.gov/Mission/> for more details.

105 MISR employs two processing pathways for aerosol retrievals, one for observations over  
106 land (Martonchik et al., 2009), and another for dark water (DW) (Kalashnikova et al., 2013),  
107 which applies over deep oceans, seas, and lakes. Previous versions of the MISR aerosol  
108 product were extensively validated over the years (e.g., Kahn et al., 2010; Kahn and Gaitley,  
109 2015; Kalashnikova et al., 2013; Shi et al., 2014; Witek et al., 2013) showing high retrieval  
110 quality over land and ocean.

111 The current operational version of the MISR aerosol product, designated as version 23  
112 (V23), was released publicly in June 2018. It introduced multiple algorithmic, data product, and  
113 data usability improvements (Garay et al., 2020; Witek et al., 2018a, 2018b). V23 provides  
114 aerosol information with a spatial resolution of 4.4 km x 4.4 km packaged in NetCDF-4 format.  
115 Initial validation efforts showed that V23 retrievals are more accurate than previous versions,  
116 with most pronounced improvements in the DW algorithm (Garay et al., 2020). V23 retrievals  
117 over oceans were extensively validated by Witek et al. (2019), indicating excellent agreement  
118 with ground-based observations. Other V23 Aerosol Optical Depth (AOD) evaluation efforts  
119 show similar results (e.g., Choi et al., 2019; Sayer et al., 2020; Si et al., 2020; Sogacheva et al.,  
120 2020). A first regional insight into retrieved particle properties from the MISR V23 aerosol  
121 product shows that MISR generally captures the distinct spatial and temporal features of aerosol  
122 type in East Asia (Tao et al., 2020). Furthermore, V23 has greatly improved the quality of  
123 reported AOD uncertainties, which now realistically represent retrieval errors (Sayer et al., 2020;  
124 Witek et al., 2019). This is especially relevant as pixel-level retrieval uncertainties are very  
125 important for satellite data assimilation, which is being increasingly used in aerosol modeling  
126 studies (Lynch et al., 2016; Shi et al., 2011, 2013; Zhang and Reid, 2010). MISR data and  
127 related documentation can be obtained from: <https://asdc.larc.nasa.gov/project/MISR>.

128

### 129 **3. NRT latency and data description**

130

131 MISR currently provides several L1 and L2 near real-time (NRT) radiance and cloud motion  
132 vector products (<https://earthdata.nasa.gov/earth-observation-data/near-real-time/download-nrt->

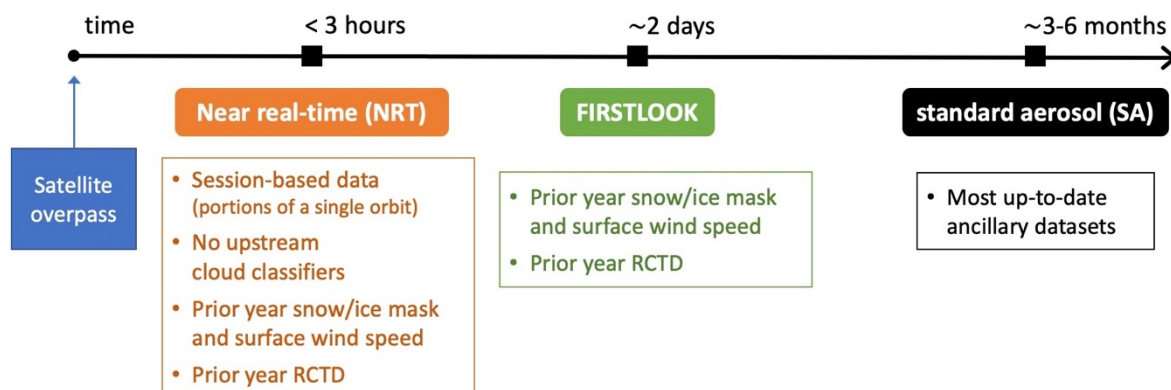
133 [data/misr-nrt](#)). All MISR NRT processing is based on Level 0 data downlinked in observational  
134 sessions. These session-based files, representing portions of a single MISR orbit, usually cover  
135 between 10 to 50 minutes of observations, as compared to the full orbit period of 98.9 minutes.  
136 This session-based processing is necessary to allow for the fast product delivery required for  
137 NRT applications.

138 The new NRT L2 aerosol product file content, described in Data Product Specification  
139 ([https://asdc.larc.nasa.gov/documents/misr/DPS\\_AEROSOL\\_NRT\\_V023.20210430.pdf](https://asdc.larc.nasa.gov/documents/misr/DPS_AEROSOL_NRT_V023.20210430.pdf)), is  
140 equivalent to the standard aerosol product (Garay et al., 2020). The NRT L2 aerosol product file  
141 name convention is:

142 MISR\_AM1\_AS\_AEROSOL\_T{yyyymmddHHMMSS}\_P{ppp}\_O{ooooo}\_F13\_0023.nc, where  
143 'yyyy', 'mm', and 'dd' are the year, month, and day, and 'HH', 'MM' and 'SS' are the hour,  
144 minute, and seconds, respectively. Furthermore, {ppp} is the three-digit path identifier (between  
145 001 and 233) and {ooooo} is the six-digit orbit number. The NRT L2 aerosol product files are  
146 available for download within three hours of acquisition at NASA's Atmospheric Science Data  
147 Center (ASDC) (<https://asdc.larc.nasa.gov/project/MISR>).

148 For clarity, it is important to distinguish between the three different MISR L2 aerosol  
149 products: NRT, FIRSTLOOK, and standard aerosol (SA) product (see Figure 1). NRT is  
150 generated within a three-hour time interval after acquisition and uses the same ancillary inputs  
151 as FIRSTLOOK. These include the monthly gridded (1.0 degree) snow/ice mask and surface  
152 wind speed from the Terrestrial Atmospheric and Surface Climatology (TASC) database and the  
153 seasonal Radiometric Camera-by-camera Threshold Dataset (RCTD) (Diner et al., 1999a). Both  
154 NRT and FIRSTLOOK utilize TASC and RCTD datasets from the current month/season in the  
155 prior year. The FIRSTLOOK product is generated within two days from acquisition and includes  
156 cloud classification parameters obtained from the L1 and L2 cloud products. The SA product is  
157 available after final processing is performed on a seasonal basis and within three months past  
158 the end of the season, which results in a 3–6-month latency. The final processing utilizes the  
159 most recent snow/ice and wind speed data.

## MISR aerosol product production sequence



160  
 161 Figure 1 Schematic showing MISR aerosol product delivery timeline. Snow/ice mask and surface wind speed data are monthly  
 162 averages. RCTD stands for Radiometric Camera-by-camera Threshold Dataset. MISR final production (SA) is processed on a  
 163 seasonal cycle and is often delayed one to three months past the end of each season, which results in up to 6-month latency.  
 164

### 165 4. Cloud screening in the NRT MISR aerosol product

#### 166 4.1. Cloud identification

167  
 168  
 169 Identification of cloudy pixels is a critical element of all satellite aerosol remote sensing  
 170 algorithms. MISR employs several cloud identification strategies which can be loosely split into  
 171 two groups: the first group relies on cloud classifiers previously generated with MISR Level 2  
 172 Cloud Detection and Classification algorithm (Diner et al., 1999b), and the second group  
 173 includes build-in tests that are internal to the aerosol retrieval algorithm (Diner et al., 2008).  
 174

##### 175 4.1.1. Upstream cloud classifiers

176  
 177 The operational MISR aerosol algorithm relies on a range of external input datasets that are  
 178 either static—for example, a monthly wind speed climatology—or that need to be generated  
 179 prior to aerosol retrievals in upstream processing. A notable example of such external inputs to  
 180 the SA and FIRSTLOOK algorithms are cloud classification parameters obtained from the MISR  
 181 L2 cloud product. An important implication of this dependency is that aerosol processing needs  
 182 to wait for the cloud product to be generated, creating a time lag that is prohibitive for NRT  
 183 applications. Typically, the L2 cloud product is generated within about 18 hours of overpass,

184 and the MISR L2 FIRSTLOOK aerosol processing is completed within about 2 days. In order to  
185 produce an L2 aerosol product within an about three-hour time frame, the algorithm needs to  
186 operate without the upstream cloud classifiers.

187 Two specific L2 cloud classification parameters utilized in FIRSTLOOK and SA aerosol  
188 processing are the MISR Stereoscopically-Derived Cloud Mask (SDCM) and the Angular  
189 Signature Cloud Mask (ASCM) (Diner et al., 1999b; Girolamo and Davies, 1994). In addition to  
190 these L2 products, the Radiometric Camera-by-camera Cloud Mask (RCCM) (Diner et al.,  
191 1999a; Girolamo and Davies, 1995) retrieved in L1B processing is also employed. All three  
192 parameters are reported at 1.1 km x 1.1 km resolution. It should be noted that RCCM also  
193 serves as an input to the algorithm that generates SDCM and ASCM, indicating that these  
194 parameters are not independent.

195 In the FIRSTLOOK and SA algorithm, the RCCM, SDCM, and ASCM cloud masks are  
196 used together to determine whether a particular 1.1 km x 1.1 km subregion is clear or cloudy.  
197 The implication is that if any of the 9 MISR cameras is designated as cloudy in a subregion, this  
198 subregion is excluded from aerosol retrieval. The clear/cloudy decision logic depends on the  
199 underlying surface type, assigned into three categories: land, water, and snow/ice. Generally, a  
200 “clear” outcome is favored over the two most frequently used surface types, land and water,  
201 assigning a subregion as cloudy only if the RCCM and SDCM masks indicate a cloud. The logic  
202 is considerably more conservative over snow/ice surfaces due to difficulties in distinguishing  
203 clouds from the underlying bright features. Details of the cloud mask decision logic over different  
204 surface types can be found in Diner et al. (2008).

205 Analyzing three months of V23 L2 SA product (March, April, May, 2020) indicates that  
206 the cloud masks along with the brightness test (see 4.1.2) lead to screening of about 50% of  
207 retrievals. As such, they have the largest impact on identifying and removing pixels where  
208 clouds might be present. These masks and decision pathways, however, have their deficiencies  
209 and additional checks were put in place to further decrease the frequency of cloud-  
210 contaminated aerosol retrievals.

211

#### 212 **4.1.2. Built-in cloud detection methods**

213

214 In addition to the cloud masks retrieved in the L1B processing (RCCM) and from the L2 Cloud  
215 Detection and Classification algorithm (SDCM, ASCM), the MISR aerosol retrieval algorithm  
216 relies on three internal tests to further identify cloudy pixels that might have escaped earlier  
217 detection. These are (1) the *brightness test*, (2) the *angle-to-angle smoothness test*, and (3) the

218 *angle-to-angle correlation test*. Details of these tests can be found in Martonchik et al. (2002) or  
219 Diner et al. (2008), but a short summary is provided here for completeness.

220 The brightness test is employed to identify clouds that lacked sufficient texture to be  
221 picked up by SDCM. For each surface type a fixed threshold is adopted on measured  
222 bidirectional reflectance factors (BRFs), and when exceeded in all spectral bands for at least  
223 one camera, it renders a subregion unsuitable for aerosol retrieval. The thresholds are set to  
224 1.0, 0.5, and 0.5 for snow/ice, land, and water surfaces, respectively. The value of 1.0 means  
225 that the brightness test is effectively turned off over snow/ice. Furthermore, the brightness test  
226 does not override subregions that were identified as clear by RCCM.

227 The angular smoothness test checks for unusually large variations in the measured  
228 equivalent reflectances as a function of camera angle, the premise being that in the absence of  
229 artifacts or subpixel clouds, the measured radiance should change smoothly from camera to  
230 camera. The test is achieved by fitting a polynomial to equivalent reflectances, separately for aft  
231 (+nadir) and forward (+nadir) cameras and each spectral band, and checking if the goodness of  
232 fit metric (definition in Diner et al., 2008) exceeds a threshold. If in at least one case the test  
233 fails, the subregion is eliminated.

234 Finally, the angle-to-angle correlation test also investigates radiance smoothness and  
235 correlation between camera angles, which makes it conceptually similar to the angular  
236 smoothness test, but instead utilizes high-resolution information from the red spectral band. It  
237 uses 4 x 4 arrays of the 275m spatial resolution red band equivalent reflectances in each 1.1 km  
238 x 1.1 km subregion. The test then evaluates spatial variability within the 4 x 4 array for each  
239 camera and compares it to a variability within a camera-average template. Variances,  
240 covariances, and normalized cross-correlations are calculated (see Diner et al., (2008) for  
241 details). If the variability within a camera deviates considerably from the average, this camera  
242 might have sub-pixel clouds or other contaminants, and as a result the subregion is excluded  
243 from aerosol retrievals.

244 In the three months of data analyzed in this study (March, April, May 2020), the relative  
245 occurrence of retrieval screening due the above-mentioned internal tests are about 4.0% and  
246 0.1% for the correlation and smoothness tests, respectively. These statistics come from  
247 analyzing the output field *Aerosol\_Retrieval\_Screening\_Flags* and as such they do not  
248 represent the absolute rates of success of each individual test. That is because the tests are  
249 performed sequentially, and if one fails, subsequent tests are not performed. For SA product  
250 generation, the order is: upstream cloud mask described in 4.1.1, the brightness test, the  
251 correlation test, and the smoothness test. For example, the correlation test is only performed on



252 pixels that already passed the upstream cloud tests as well as the brightness test. Additionally,  
253 the brightness test does not have its own flag in the *Aerosol\_Retrieval\_Screening\_Flags* output  
254 but is grouped together with the upstream cloud classifiers.

255

## 256 **4.2. Retrieval screening using regional cloud parameters**

257

258 Methods described in section 4.1 focus on identifying and excluding cloudy 1.1 km x 1.1 km  
259 subregions from the aerosol retrieval process. The retrieval region consists of 16 (4 x 4)  
260 subregions. These methods are highly effective at removing cloud-contaminated pixels, but  
261 since they rely on MISR visible wavelengths they might miss certain cloud signatures more  
262 easily detected in the infrared spectrum (e.g., Gao et al., 1993). For example, MODIS routinely  
263 uses its reflective and emissive infrared channels to detect optically thin cirrus clouds  
264 (Ackerman et al., 2010; Levy et al., 2013). As a result, MISR cloud detection methods  
265 occasionally fail, which leads to visible outliers in retrieved AODs (Witek et al., 2018b). For that  
266 reason, an additional set of screenings is applied in an effort to eliminate such unusually high  
267 AOD retrievals (Garay et al., 2020). Two of these additional methods look at overall cloudiness  
268 in the retrieval region (consisting of 4 x 4 subregions) as well as in a larger area consisting of 3  
269 x 3 regions (12 x 12 subregions). The Cloud Screening Parameter (CSP) represents the fraction  
270 of clear grid cells within a region, whereas Cloud Screening Parameter Neighbor 3x3 (CSP9) is  
271 similar to CSP but for the larger area. If CSP is below 0.7 and CSP9 below 0.5, the retrieval is  
272 not reported in the final product intended for most users. However, it is still included in the  
273 product's AUXILIARY subcategory and annotated with the term "Raw" to indicate that the  
274 product has not passed the recommended quality screenings.

275

## 276 **4.3. Adjusting cloud screening thresholds**

277

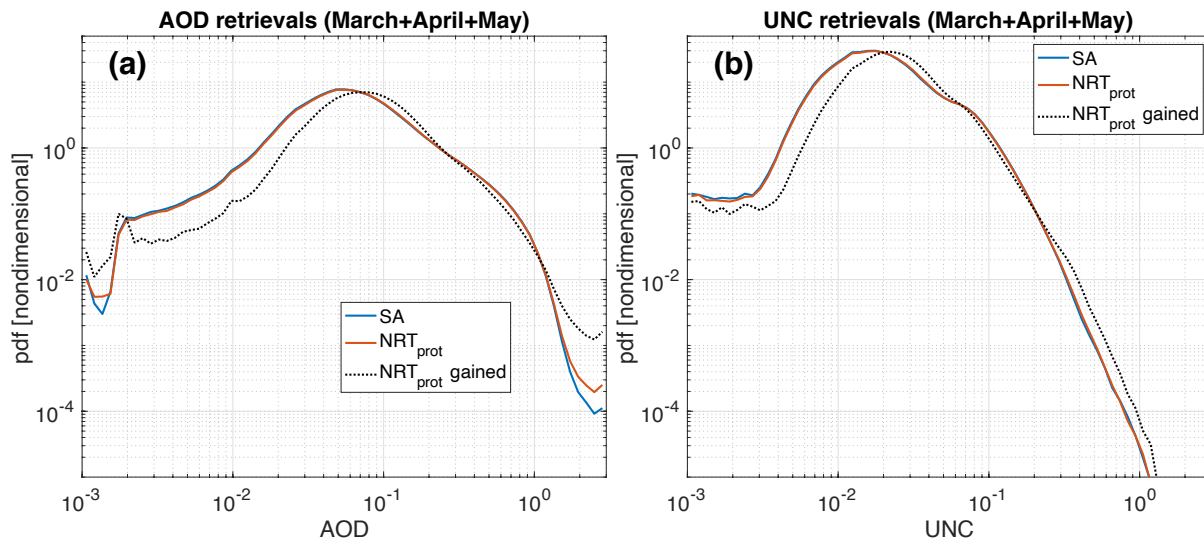
### 278 **4.3.1. Performance of the prototype NRT product**

279

280 This subsection presents results and analysis of prototype NRT aerosol retrievals. These are  
281 obtained prior to any threshold and screening adjustments included in the final version of the  
282 product. To differentiate between the final and the prototype NRT products, the latter is denoted  
283 as  $NRT_{prot}$ .

284 As mentioned in the previous section, the NRT processing cannot rely on the cloud  
285 masks generated in the L1 and L2 cloud products, namely the RCCM, SDCM, and ASCM. This

286 implies that potentially less screening of cloudy subregions would be applied, increasing the  
 287 probability of cloud contamination in aerosol retrievals. However, some of the burden of cloud  
 288 identification is picked up by the built-in cloud tests described in section 4.1.2. The frequency of  
 289 these tests identifying cloudy pixels increases in NRT processing in comparison to standard  
 290 processing, in large part mitigating the negative consequences resulting from the lack of the  
 291 upstream cloud masks. This is well evidenced by examining the normalized probability density  
 292 functions (*pdfs*) of AOD from spring 2020 (Figure 2). The SA (red) and NRT<sub>prot</sub> (blue) lines are  
 293 very similar, indicating that the built-in cloud tests substitute to a significant extent for the  
 294 missing upstream cloud masks in generating the NRT<sub>prot</sub> product. The largest difference occurs  
 295 in the high-AOD range, suggesting that NRT<sub>prot</sub> has more retrievals in this regime. The black  
 296 dotted line shows a *pdf* of the NRT<sub>prot</sub> AOD retrievals that do not have a matching SA retrieval.  
 297 This is labeled as “NRT<sub>prot</sub> gained” as it represents additional retrievals obtained in NRT  
 298 processing due to the lack of external cloud masks. The “NRT<sub>prot</sub> gained” *pdf* is clearly shifted  
 299 towards higher AODs, confirming that the NRT<sub>prot</sub> processing tends to retrieve higher AODs in  
 300 places where SA is not available.

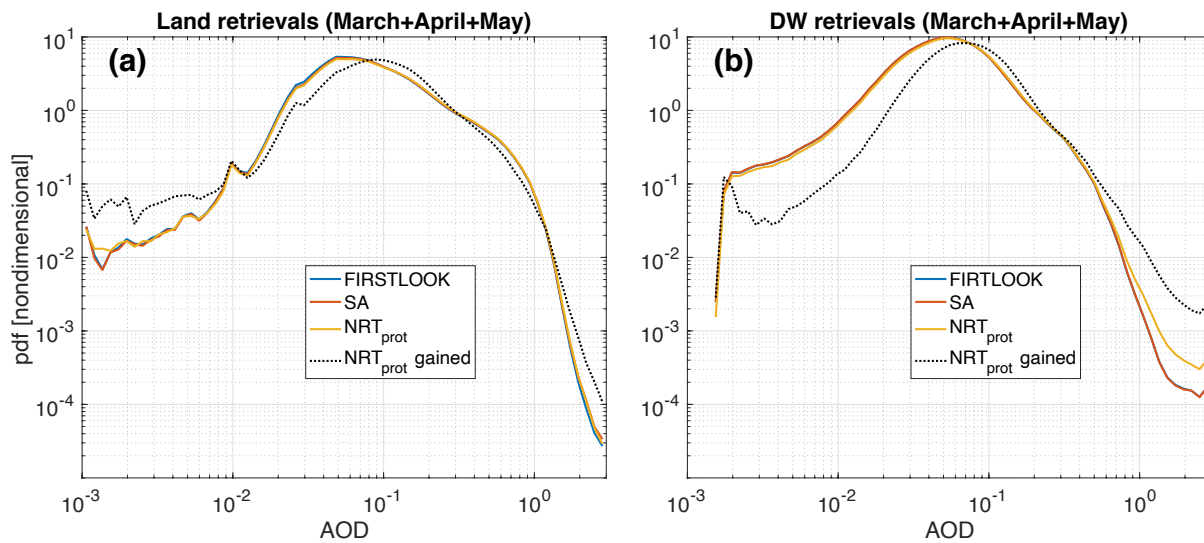


301  
 302 *Figure 2 (a) AOD normalized probability density functions from SA, prototype NRT, and prototype NRT retrievals that do not*  
 303 *have a matching SA equivalent (labeled as NRT<sub>prot</sub> gained); (b) same as in (a) but for retrieved AOD uncertainties (UNC). Data*  
 304 *statistics for AODs are provided in Table 1.*

305 Figure 3 shows *pdfs* of AOD but with retrievals separated between DW (Fig. 3a) and  
 306 land (Fig. 3b). These *pdfs* indicate that the retrievals over oceans are the main source of  
 307 increased frequency of high-AODs in the NRT<sub>prot</sub> product. The *pdfs* over land are virtually  
 308 unchanged, including a slightly flattened but still relatively comparable distribution of the “NRT<sub>prot</sub>

309 gained” retrievals (Fig. 3b). The additional statistics of the data presented in Figs. 2 and 3,  
 310 including the retrieval count, the mean AOD, and the geometric mean AOD, which is better  
 311 suited for log-normal distributions of AOD (Sayer and Knobelspiesse, 2019), are provided in  
 312 Table 1. Note that the number of  $NRT_{prot}$  gained is not the same as the number of  $NRT_{prot}$  minus  
 313 SA. This is because some SA retrievals do not have their  $NRT_{prot}$  equivalent, making the SA  
 314 count larger than it would have been otherwise.

315 In the 3-month period analyzed in this study (March, April, May, 2020), the  $NRT_{prot}$   
 316 processing leads to about 6.4% more retrievals than SA (see Table 1). 5.5 million  $NRT_{prot}$   
 317 retrievals do not have a matching SA retrieval ( $NRT_{prot}$  gained), and the majority of them (67%) are  
 318 DW retrievals. The overall geometric means are almost identical in SA and  $NRT_{prot}$ , although  
 319 small variations in this statistic are seen in DW and land categories. The  $NRT_{prot}$  gained have  
 320 visibly higher arithmetic and geometric mean values, the increase coming mainly from DW  
 321 retrievals. These basic statistics warrant a further look at the  $NRT_{prot}$  performance over DW.



322  
 323 Figure 3 AOD pdfs for land (a) and DW (b) retrievals, respectively. Data statistics are provided in Table 1.

	All retrievals			DW			Land		
	SA	$NRT_{prot}$	$NRT_{prot}$ gained	SA	$NRT_{prot}$	$NRT_{prot}$ gained	SA	$NRT_{prot}$	$NRT_{prot}$ gained
$N (\times 10^6)$	49.7	52.9	5.5	27.6	30.7	3.7	22.1	22.2	1.8
<i>mean</i>	0.168	0.169	0.171	0.111	0.115	0.146	0.240	0.243	0.224

<i>geomean</i>	0.111	0.112	0.122	0.083	0.085	0.106	0.160	0.162	0.161
----------------	-------	-------	-------	-------	-------	-------	-------	-------	-------

324 *Table 1 Additional statistics for the data presented in Figs. 2 and 3 (statistic for FIRSTLOOK not shown). NRT gained stands for*  
325 *the prototype NRT retrievals that do not have a matching SA equivalent; geomean stands for the geometric mean AOD.*

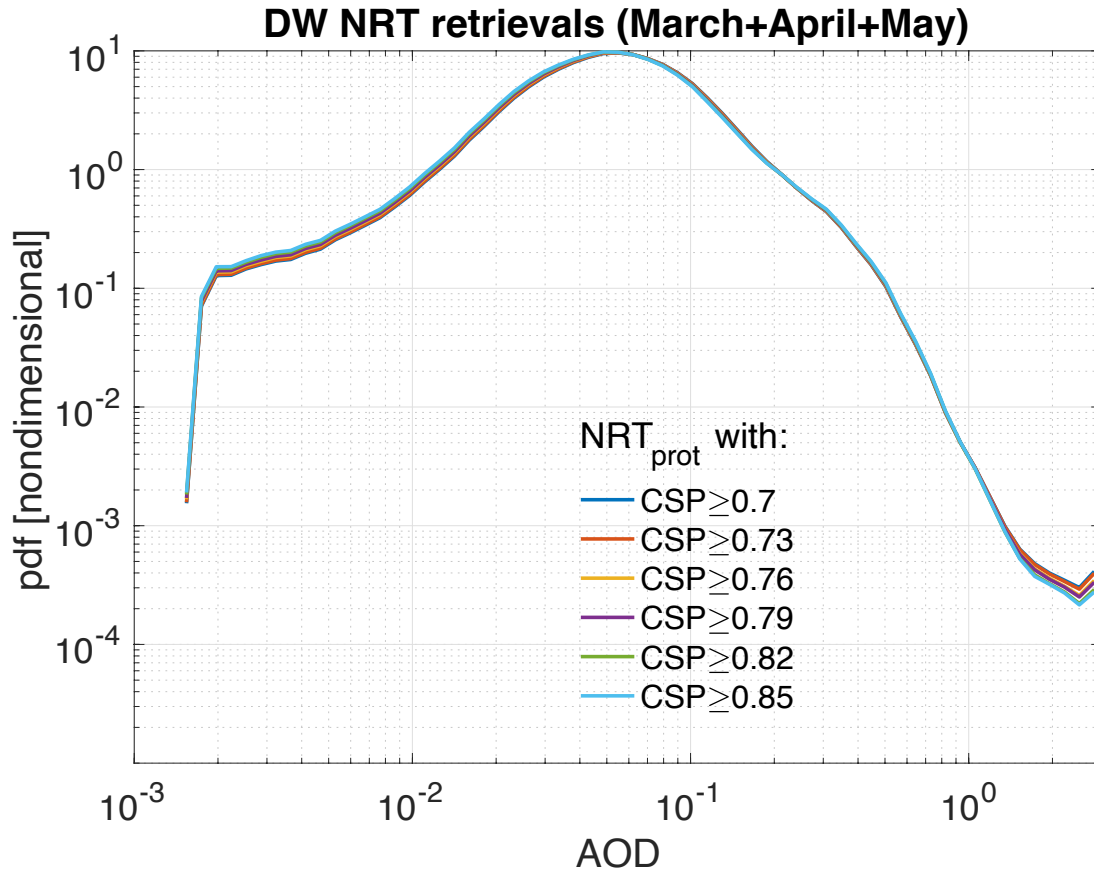
326

### 327 **4.3.2. Sensitivity to CSP and CSP9 thresholds in DW retrievals**

328

329 One way to screen potentially cloud-contaminated high-AOD retrievals is to adjust thresholds on  
330 CSP and CSP9 parameters (Garay et al., 2020). This is furthermore justified by the fact that in  
331 the absence of RCCM, SDCM, and ASCM in NRT<sub>prot</sub> processing, fewer cloudy subregions are  
332 identified in a retrieval area and consequently CSP and CSP9 have by default lower values.  
333 This argument provides strong justification for investigating sensitivity to increased CSP and  
334 CSP9 thresholds in the NRT<sub>prot</sub> processing.

335 The SA product uses the thresholds of CSP=0.7 and CSP9=0.5 (Garay et al., 2020);  
336 when the values of CSP and CSP9 are below these thresholds in a retrieval region, the aerosol  
337 retrieval is removed from the data field recommended for users. Figure 4 and Table 2 show *pdfs*  
338 and AOD statistics for different thresholds of CSP and CSP9 parameters in the NRT<sub>prot</sub> product  
339 over dark water surfaces. There are only minor changes in the *pdfs* when the thresholds are  
340 increased, including in the high-AOD regime. The arithmetic and geometric mean values  
341 decrease slowly; even at the highest considered thresholds (0.85 for CSP and 0.75 for CSP9)  
342 these statistics are still above the SA values. At the same time the number of passing NRT<sub>prot</sub>  
343 retrievals decreases considerably faster, with almost 19% of retrievals lost when the highest  
344 thresholds are used. These results indicate that adjusting CSP and CSP9 thresholds is not an  
345 effective strategy to constraining NRT<sub>prot</sub> retrievals.



346  
 347 *Figure 4 Prototype NRT AOD pdfs over dark water surfaces from spring 2020 obtained with different CSP and CSP9 cloud-*  
 348 *screening thresholds. Data statistics are provided in Table 2.*

$N (\times 10^6)$	30.7	30.1 (-1.9%)	28.4 (-7.4%)	27.7 (-9.8%)	25.9 (-15.6%)	24.9 (-18.9%)	SA 27.6
<i>CSP</i>	$\geq 0.7$	$\geq 0.73$	$\geq 0.76$	$\geq 0.79$	$\geq 0.82$	$\geq 0.85$	
<i>CSP9</i>	$\geq 0.5$	$\geq 0.55$	$\geq 0.6$	$\geq 0.65$	$\geq 0.7$	$\geq 0.75$	
<i>mean</i>	0.1151 $\pm 0.1200$	0.1149 $\pm 0.1199$	0.1145 $\pm 0.1190$	0.1144 $\pm 0.1191$	0.1142 $\pm 0.1185$	0.1143 $\pm 0.1189$	0.1110 $\pm 0.1079$
<i>geomean</i>	0.0850	0.0847	0.0841	0.0839	0.0834	0.0832	0.0826

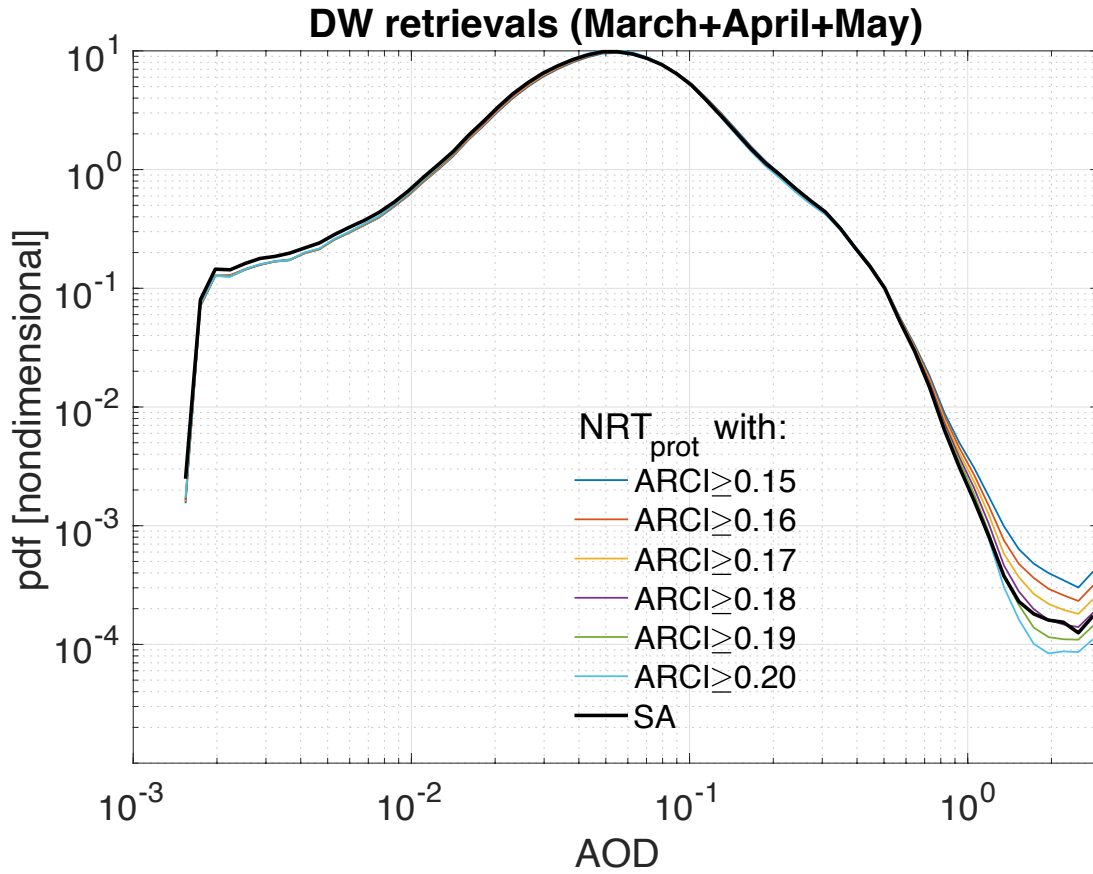
349 *Table 2 Additional statistics for the data presented in Fig. 4. Values for CSP and CSP9 indicate their corresponding thresholds for*  
 350 *screening AOD retrievals. The arithmetic mean values are accompanied by their respective  $\pm$  one standard deviations.*

351  
 352 **4.3.3. Sensitivity to ARCI threshold in DW retrievals**

353

354 V23 of the MISR aerosol product introduced a new parameter, called the aerosol retrieval  
355 confidence index (ARCI), that is used to screen high-AOD retrieval outliers caused by cloud  
356 contamination and other factors (Witek et al., 2018b). ARCI, defined only for DW retrievals,  
357 proved to be an efficient metric at filtering out potentially cloud-contaminated AOD retrievals. In  
358 standard processing, retrievals with  $ARCI < 0.15$  are removed from the recommended user  
359 field, but are retained in the AUXILIARY group. The 0.15 threshold is well supported through  
360 statistical analysis (Witek et al., 2018b), although some erroneous results still pass this  
361 screening method, suggesting that increasing this threshold might be beneficial in NRT  
362 processing.

363 Figure 5 and Table 3 show *pdfs* and AOD statistics for different thresholds of ARCI in the  
364 NRT<sub>prot</sub> product. In this case the differences between ARCI thresholds are quite noticeable,  
365 especially in the high-AOD range of retrievals. Increasing the ARCI threshold to 0.2 leads to a  
366 loss of about 11% of NRT<sub>prot</sub> DW retrievals, but the resulting arithmetic and geometric mean  
367 values are lower than the SA values. At the same time, the absolute number of NRT<sub>prot</sub> DW  
368 retrievals (27.4 million) is still comparable to the number of SA DW retrievals (27.6 million). The  
369 *pdfs* and the statistics suggest that increasing the NRT<sub>prot</sub> ARCI threshold from 0.15 to 0.18  
370 leads to a product that has similar characteristics to SA.



371  
 372 *Figure 5 Prototype NRT AOD pdfs from spring 2020 obtained with different ARCI thresholds. Data statistic are provided in Table*  
 373 *3.*

$N (\times 10^6)$	30.7	30.0 (-2.2%)	29.4 (-4.3%)	28.7 (-6.5%)	28.0 (-8.6%)	27.4 (-10.8%)	SA 27.6
<i>ARCI</i>	$\geq 0.15$	$\geq 0.16$	$\geq 0.17$	$\geq 0.18$	$\geq 0.19$	$\geq 0.20$	
<i>mean</i>	0.1151 $\pm 0.1200$	0.1137 $\pm 0.1157$	0.1124 $\pm 0.1122$	0.1112 $\pm 0.1094$	0.1100 $\pm 0.1070$	0.1090 $\pm 0.1051$	0.1110 $\pm 0.1079$
<i>geomean</i>	0.0850	0.0842	0.0835	0.0828	0.0821	0.0813	0.0826

374 *Table 3 Additional statistic for the data presented in Fig. 5.*

375  
 376 **4.3.4. Recommendation for NRT processing**

377  
 378 The statistical analyses presented in the previous sections indicate that the lack of RCCM,  
 379 SDCM, and ASCM in NRT processing has negative consequences on the product, especially by

380 allowing more, potentially cloud-contaminated, high-AOD DW retrievals to pass screening  
381 criteria. Adjusting build-in cloud screening thresholds on CSP and CSP9 brings only limited  
382 benefits at the cost of losing a considerable percentage of retrievals. However, the ARCI  
383 threshold adjustments result in much closer statistical correspondence between the  $NRT_{prot}$  and  
384 standard AOD retrievals. For that reason, a revised ARCI threshold of 0.18 is implemented in  
385 NRT processing. Since the unscreened retrievals, as well as the ARCI parameter, are also  
386 provided in the AUXILIARY group of the product, users are encouraged to experiment with their  
387 own thresholds which might prove more beneficial in specific applications or geographic areas.

388

#### 389 **4.4. Cloud/clear decision logic over snow/ice**

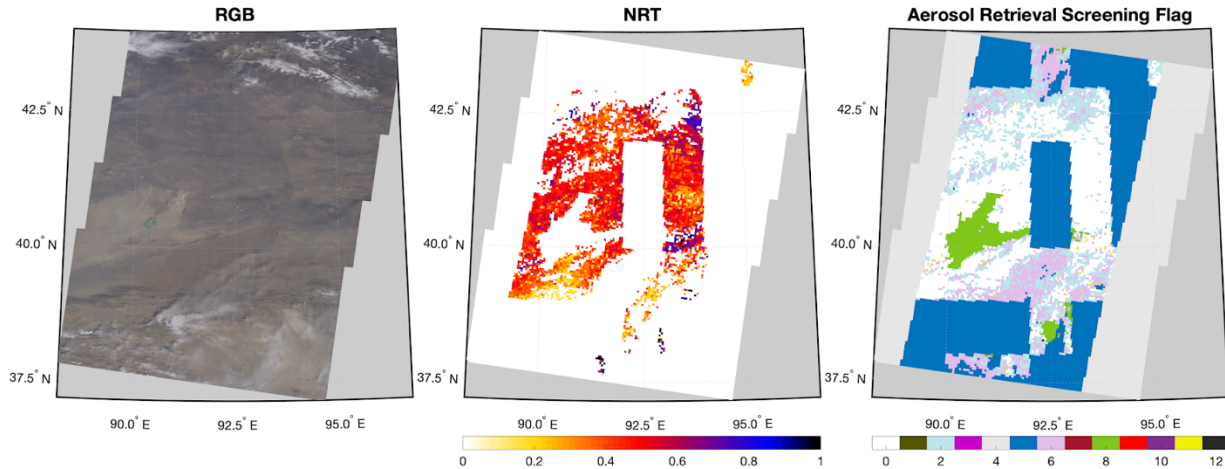
390

391 In section 4.1.1 the impact of upstream cloud classifiers in standard processing—namely the  
392 RCCM, SDCM, and ASCM—on the subregion’s cloud/clear designation was briefly described.  
393 The decision pathway depends on the underlying surface type, which can be either land, water,  
394 or snow/ice. Over land and water, the “cloud” outcome is only obtained when both RCCM and  
395 SDCM designate the subregion as cloudy. In the absence of RCCM and SDCM the default  
396 outcome is “clear”. Over snow/ice, however, the logic is more restrictive and favors the “cloudy”  
397 designation (Diner et al., 2008). Specifically, when the upstream cloud classifiers are not  
398 available, the subregion designation is set to “cloudy” by default. This has important implications  
399 on aerosol retrievals in areas where snow and ice occur seasonally.

400 The snow/ice surface mask, unlike land and water, is not static and changes every  
401 month. Furthermore, the snow/ice mask input to MISR aerosol processing has a 1.0-degree  
402 horizontal resolution, which is re-gridded to a 1.1 km resolution corresponding to the resolution  
403 of MISR subregion. In FIRSTLOOK processing, the snow/ice mask from the same month but in  
404 the previous year is used. The final SA processing is performed when the current year’s monthly  
405 snow/ice mask becomes available. The NRT processing, similarly to FIRSTLOOK, relies on the  
406 previous year’s snow/ice mask. Additionally, given the lack of upstream cloud classifiers, the  
407 snow/ice areas are designated as “cloudy” for aerosol retrieval purposes. This is well visualized  
408 in Figure 6 which shows the visible image and the corresponding maps of AOD and Aerosol  
409 Retrieval Screening Flag in the NRT processing. The dark blue color (index 5) denotes cloudy  
410 regions determined using the snow/ice cloud logic. The box-like nature of the excluded areas is  
411 associated with the coarse resolution of the snow/ice mask (1.0 degree). The previous year’s  
412 mask might also not be representative of the current conditions on the ground. It is worth noting  
413 that the FIRSTLOOK product often suffers from the same exclusion rules as NRT. This is



414 because of the strict clear/cloud logic over snow/ice surfaces which favors the cloudy outcome;  
415 in the case shown in Fig. 6 the AOD gaps in FIRSTLOOK (not shown) look very similar to the  
416 NRT product.



417  
418 *Figure 6 Example of snow/ice masking in NRT AOD retrievals. (Left) Visible image of the retrieval area. (Center) Corresponding*  
419 *NRT AOD retrievals. (Right) NRT Aerosol Retrieval Screening Flag for the same area; the dark blue color denotes regions*  
420 *designated as cloudy.*

421 Several attempts have been made by the MISR science team to improve NRT aerosol  
422 retrievals in snow/ice covered areas. However, identifying and isolating snow-covered surfaces  
423 in the absence of upstream cloud classifiers proves very challenging. The quality of aerosol  
424 retrievals is often negatively affected in such conditions. For that reason, and in an attempt to  
425 eliminate as many NRT AOD outliers as possible, the current snow/ice logic is retained in the  
426 NRT aerosol processing.

427

## 428 **5. NRT and SA product comparisons**

429

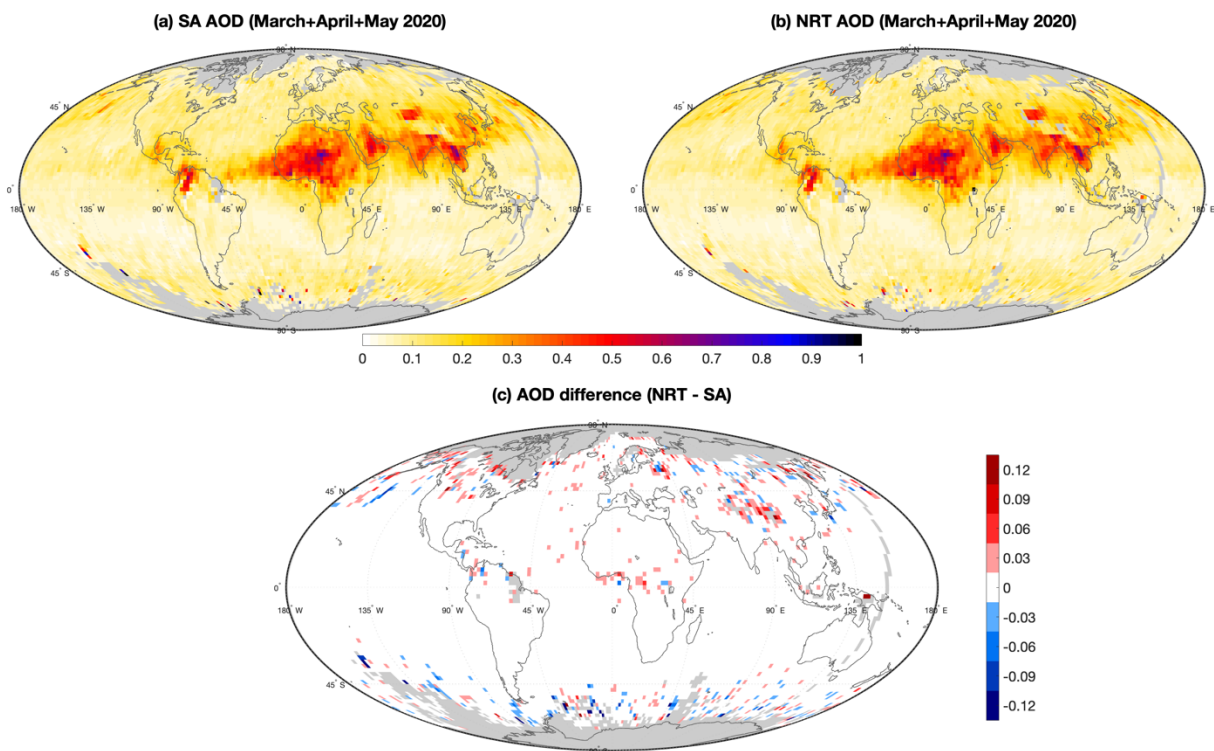
### 430 **5.1. Total AOD**

431

432 In this section, geographic distributions of MISR AOD retrievals from SA and NRT products are  
433 analyzed. The datasets encompass three months, March, April, and May of 2020. The NRT  
434 retrievals are screened with the revised ARCI threshold of 0.18 as suggested in section 4.3.4.  
435 The spatial overlap of the SA and NRT data is achieved using an intersect of the X\_Dim and  
436 Y\_Dim fields in the two data products.

437 Figure 7 shows the global distributions of geometric mean AOD from the (a) SA and (b)  
 438 NRT products. The retrievals are gridded at 2-by-2-degree spatial resolution. Fig. 7c shows the  
 439 AOD difference between the two products (NRT – SA).

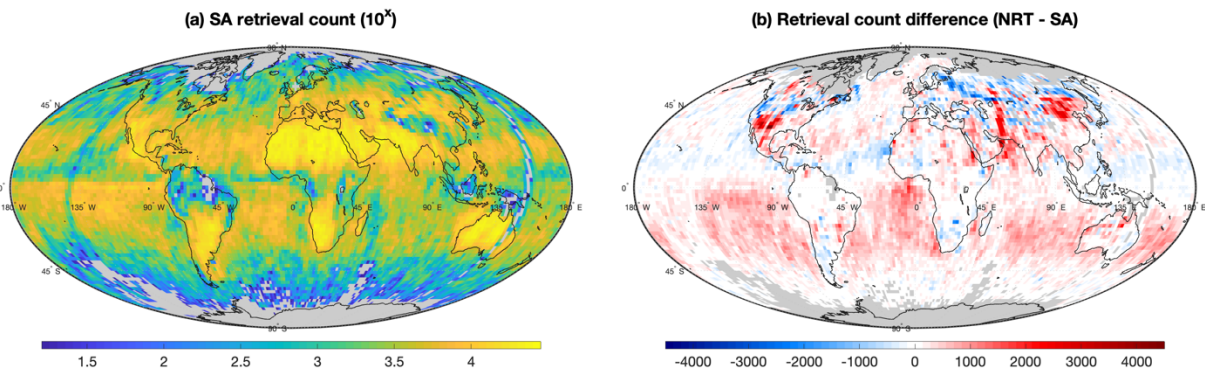
440 The largest AOD differences are seen in areas with climatologically high cloud cover,  
 441 especially over the Southern Ocean, and over land in areas where potential snow cover could  
 442 be an issue. Over the Southern Ocean the SA AODs are predominantly higher than the NRT  
 443 AODs. This is due to the increased ARCI threshold in NRT (0.18 vs. 0.15 in SA) which brings in  
 444 more aggressive screening of cloud-contaminated retrievals (Witek et al., 2018b). Over land,  
 445 where the ARCI parameter is not available, the gridded NRT AODs tend to be higher than the  
 446 SA AODs, which is in part related to the differences in snow/ice mask between the two  
 447 products. Still, the AOD differences in Fig. 7c are rather small and reflect sampling issues rather  
 448 than any systematic deficiencies in NRT processing. At the same time the lack of cloud  
 449 classifiers in NRT does not adversely affect AOD distributions, which is consistent with the  
 450 statistical analysis presented in section 4.2.3.



451  
 452 *Figure 7 (a) Global distribution of SA AOD geometric mean values across March, April, and May of 2020 on a 2-by-2-degree*  
 453 *spatial resolution; (b) same as in (a) but for NRT AOD; and (c) AOD difference between SA and NRT. Grid points with less than 15*  
 454 *retrievals are excluded.*

455 **5.2. Retrieval yields**

456 Figure 8 complements Fig. 7 by showing (a) the SA retrieval count distribution as well as (b) the  
457 retrieval count difference between the SA and NRT products.



458  
459 *Figure 8 (a) Decimal logarithm of the retrieval count from the SA product in March, April, and May of 2020; (b) retrieval count*  
460 *difference between SA and NRT. Presented values are gridded at 2-by-2-degree spatial resolution and grid points with less than*  
461 *15 retrievals are excluded.*

462 The highest number of retrievals is found over the subtropical continents where the  
463 cloud cover is usually the smallest. Over the subtropical oceans in the Southern Hemisphere the  
464 NRT retrieval counts are typically higher than in SA, which results from the absence of upstream  
465 cloud classifiers in NRT processing and subsequently fewer subregions being excluded as  
466 cloudy. Note that this increase in retrieval count caused by the lack of cloud classifiers is not  
467 compensated by the increased ARCI threshold in NRT processing ( $\text{ARCI} \geq 0.18$ ), which always  
468 reduces the number of retrievals when compared to the default SA threshold ( $\text{ARCI} \geq 0.15$ ). The  
469 lack of hemispheric symmetry in this case is likely due to the seasonal variability (only months in  
470 northern spring are analyzed here). Over land the lack of upstream cloud classifiers also results  
471 in higher number of NRT retrievals in certain regions, but the surface type exclusion rules  
472 reverse this pattern, especially at higher latitudes. The conservative cloud logic over snow/ice  
473 surfaces in NRT processing often results in the lower number of NRT retrievals in the high  
474 latitudes of the northern hemisphere.

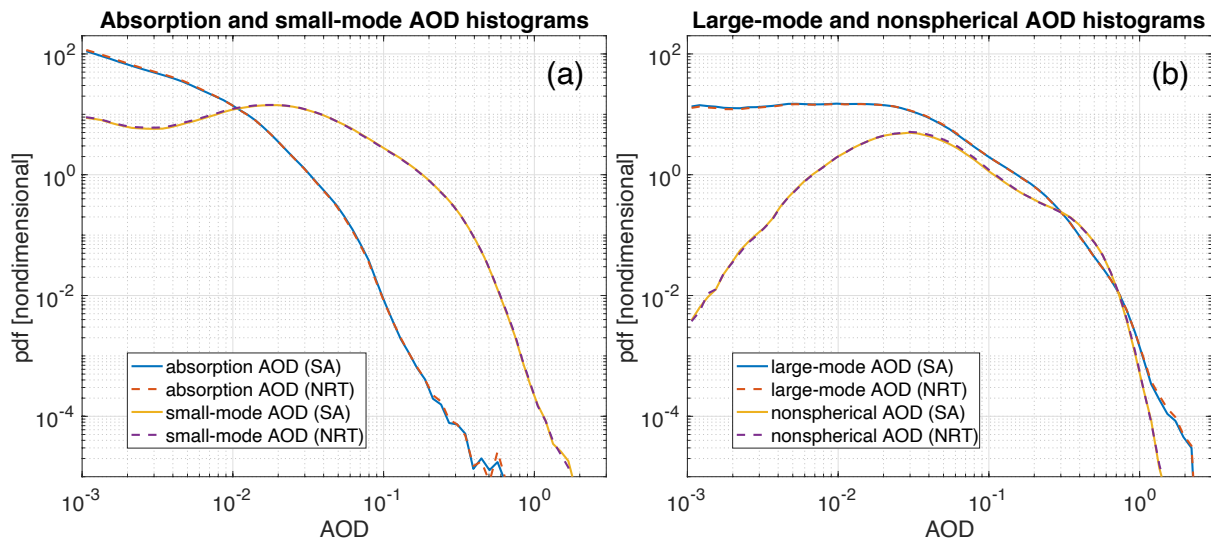
475 A metric relevant to the potential use of the NRT product in data assimilation is the  
476 retrieval yield per model grid point. The retrieval yield can be measured as, for example, the  
477 number of  $1^\circ \times 1^\circ$  grid cells that have at least 15 valid satellite retrievals in them. From this  
478 perspective, the NRT product has a retrieval yield that is about 0.7% higher than the SA  
479 product, based on the three months of data analyzed in this study.

480

### 481 **5.3. Fractional AOD**

482

483 MISR's multi-angle retrieval approach enables characterization of aerosol optical and  
 484 microphysical properties, such as fractional AODs associated with particle absorption,  
 485 nonsphericity, and size (see e.g., Kahn and Gaitley, 2015). This attribute of the MISR SA  
 486 product has been applied to many climate and air quality studies and inclusion of this capability  
 487 in the NRT product would benefit data assimilation for numerical prediction of atmospheric  
 488 aerosols (Benedetti et al., 2018). Consequently, this section provides preliminary statistical  
 489 comparisons of the SA and NRT absorption AOD along with small-mode, large-mode, and  
 490 nonspherical AOD. The results shown in Fig. 9 indicate that the probability density functions of  
 491 these aerosol properties in the NRT product are statistically equivalent to the SA product. This  
 492 assessment reaffirms the consistency of the NRT and SA products. Future studies will examine  
 493 geographic and statistical differences and other particle properties in more detail.



494  
 495 *Figure 9 Normalized probability density functions for select MISR particle property retrievals in March, April, and May 2020.*  
 496 *Solid lines represent SA retrievals and dashed represent NRT retrievals. (a) absorption AOD and small-mode AOD retrievals; (b)*  
 497 *large-mode AOD and nonspherical AOD retrievals. The differences between the SA and NRT products are negligible.*

498  
 499 **6. Summary**

500  
 501 The MISR V23 aerosol product, publicly available since mid-2018, is a high-resolution state-of-  
 502 the-art data product from NASA's Terra flagship mission. V23 AOD retrievals have remarkable  
 503 accuracy compared against ground-based observations (Garay et al., 2020; Tao et al., 2020;  
 504 Witek et al., 2019) and the product is more intuitive and easier to use than previous versions.  
 505 The product is available within 2 days from satellite overpass as a FIRSTLOOK version, and  
 506 within 3-to-6 months as a final science-quality SA version that employs the most up-to-date

507 ancillary datasets. In response to the needs of operational user communities, a new MISR L2  
508 NRT aerosol product has been developed with a 3-hour latency.

509         The new NRT algorithm does not depend on the upstream cloud classifiers that are  
510 generated in L1 and L2 cloud processing. The lack of cloud classifiers is in large part mitigated  
511 by the aerosol algorithm's built-in cloud identification methods. Analysis of the prototype NRT  
512 product has shown an increased frequency of high-AOD retrievals, especially over oceans and  
513 in climatologically cloudy areas, likely due to an increase in cloud contamination. Adjusting the  
514 ARCI threshold in DW retrievals proves highly effective at eliminating some of these high-AOD  
515 outliers and improves the NRT product's statistical agreement with the SA version. The new  
516 NRT aerosol product applies an ARCI threshold of 0.18 to mitigate cloud contamination in the  
517 absence of upstream cloud masks in NRT processing. The remaining differences in statistical  
518 and geographic distributions between the NRT and SA AODs, which includes information from  
519 the L2 cloud product, are small and largely confined to areas with high cloud cover.

520         The results of this study also serve as an example of the effects of screening threshold  
521 adjustments in MISR aerosol retrievals on AOD statistics and distributions. Researchers  
522 interested in particular applications and/or specific geographic regions are encouraged to  
523 experiment with their own threshold to achieve most optimal results. The NRT aerosol product  
524 contains both the recommended product contained within the main science directory  
525 "4.4\_KM\_PRODUCTS" that has the stricter ARCI threshold ( $ARCI \geq 0.18$ ), and the unscreened  
526 product without the additional cloud and ARCI filtering designed for more experienced users,  
527 located within the AUXILIARY group.

528

## 529 **Acknowledgements**

530 This research was carried out at the Jet Propulsion Laboratory, California Institute of  
531 Technology, under a contract with the National Aeronautics and Space Administration. Support  
532 from the MISR project is acknowledged. Special thanks to Andrew Sayer, Jeffrey Reid, and one  
533 anonymous reviewer for carefully reading the manuscript and providing valuable comments. We  
534 would also like to thank Ralph Kahn for providing feedback on the manuscript.

535

## 536 **Data availability**

537 The MISR V23 SA and NRT data is publicly available and can be downloaded from  
538 <https://asdc.larc.nasa.gov/project/MISR>. MISR NRT data is not stored permanently and is only

539 available for three to six months from the time of acquisition; please contact the corresponding  
540 author to request the NRT data from the months analyzed in this study.

541

542 **Author contributions**

543 MLW conceptualized the study, performed the analyses, and prepared the manuscript. MAB  
544 processed the initial NRT data and provided technical support. All coauthors assisted with the  
545 analyses and provided feedback on the results. Furthermore, AMN, FCS, and DJD contributed  
546 to the writing and editing of the manuscript.

547

548 **Competing interests**

549 The authors declare that they have no conflict of interest.

550

551 **References:**

- 552 Ackerman, S., Richard, F., Kathleen, S., Yinghui, L., Liam, G., Bryan, B. and Paul, M.:  
553 Discriminating clear-sky from cloud with MODIS algorithm theoretical basis document  
554 (MOD35), Univ. Wisconsin - Madison, 6th Edn.(October), 129 [online] Available from:  
555 <http://citeseerx.ist.psu.edu/viewdoc/summary?doi=10.1.1.385.4885>, 2010.
- 556 Benedetti, A., Reid, J. S. and Colarco, P. R.: International cooperative for aerosol prediction  
557 workshop on aerosol forecast verification, in *Bulletin of the American Meteorological Society*,  
558 vol. 92., 2011.
- 559 Benedetti, A., Reid, J. S., Knippertz, P., Marsham, J. H., Di Giuseppe, F., Rémy, S., Basart, S.,  
560 Boucher, O., Brooks, I. M., Menut, L., Mona, L., Laj, P., Pappalardo, G., Wiedensohler, A.,  
561 Baklanov, A., Brooks, M., Colarco, P. R., Cuevas, E., Da Silva, A., Escribano, J., Flemming, J.,  
562 Huneus, N., Jorba, O., Kazadzis, S., Kinne, S., Popp, T., Quinn, P. K., Sekiyama, T. T., Tanaka,  
563 T. and Terradellas, E.: Status and future of numerical atmospheric aerosol prediction with a  
564 focus on data requirements, *Atmos. Chem. Phys.*, 18, 10615–10643, doi:10.5194/acp-18-10615-  
565 2018, 2018.
- 566 Bocquet, M., Elbern, H., Eskes, H., Hirtl, M., Aabkar, R., Carmichael, G. R., Flemming, J.,  
567 Inness, A., Pagowski, M., Pérez Camaño, J. L., Saide, P. E., San Jose, R., Sofiev, M., Vira, J.,  
568 Baklanov, A., Carnevale, C., Grell, G. and Seigneur, C.: Data assimilation in atmospheric  
569 chemistry models: Current status and future prospects for coupled chemistry meteorology  
570 models, *Atmos. Chem. Phys.*, 15(10), 5325–5358, doi:10.5194/acp-15-5325-2015, 2015.
- 571 Buchard, V., Da Silva, A. M., Colarco, P. R., Darmenov, A., Randles, C. A., Govindaraju, R.,  
572 Torres, O., Campbell, J. and Spurr, R.: Using the OMI aerosol index and absorption aerosol  
573 optical depth to evaluate the NASA MERRA Aerosol Reanalysis, *Atmos. Chem. Phys.*, 15(10),  
574 5743–5760, doi:10.5194/acp-15-5743-2015, 2015.
- 575 Buchard, V., Randles, C. A., da Silva, A. M., Darmenov, A., Colarco, P. R., Govindaraju, R.,  
576 Ferrare, R., Hair, J., Beyersdorf, A. J., Ziemba, L. D. and Yu, H.: The MERRA-2 aerosol  
577 reanalysis, 1980 onward. Part II: Evaluation and case studies, *J. Clim.*, 30(17),  
578 doi:10.1175/JCLI-D-16-0613.1, 2017.

579 Butz, A., Hasekamp, O. P., Frankenberg, C. and Aben, U.: Retrievals of atmospheric CO<sub>2</sub> from  
580 simulated space-borne measurements of backscattered near-infrared sunlight: Accounting for  
581 aerosol effects, *Appl. Opt.*, 48, 3322–3336, doi:10.1364/AO.48.003322, 2009.

582 Choi, M., Lim, H., Kim, J., Lee, S., Eck, T. F., Holben, B. N., Garay, M. J., Hyer, E. J., Saide, P.  
583 E. and Liu, H.: Validation, comparison, and integration of GOCI, AHI, MODIS, MISR, and  
584 VIIRS aerosol optical depth over East Asia during the 2016 KORUS-AQ campaign, *Atmos.*  
585 *Meas. Tech.*, 12(8), 4619–4641, doi:10.5194/amt-12-4619-2019, 2019.

586 Colarco, P., Da Silva, A., Chin, M. and Diehl, T.: Online simulations of global aerosol  
587 distributions in the NASA GEOS-4 model and comparisons to satellite and ground-based aerosol  
588 optical depth, *J. Geophys. Res. Atmos.*, 115(14), doi:10.1029/2009JD012820, 2010.

589 Diner, D. J., Beckert, J. C., Reilly, T. H., Bruegge, C. J., Conel, J. E., Kahn, R. A., Martonchik,  
590 J. V., Ackerman, T. P., Davies, R., Gerstl, S. A. W., Gordon, H. R., Muller, J. P., Myneni, R. B.,  
591 Sellers, P. J., Pinty, B. and Verstraete, M. M.: Multiangle Image Spectroradiometer (MISR)  
592 instrument description and experiment overview, *IEEE Trans. Geosci. Remote Sens.*, 36(4),  
593 1072–1087, 1998.

594 Diner, D. J., Di Girolamo, L. and Clothiaux, E. E.: Level 1 Cloud Detection Algorithm  
595 Theoretical Basis, *Jet Propuls. Lab. Calif. Inst. Technol.*, D-13397(Rev. B), 1999a.

596 Diner, D. J., Davies, R., Di Girolamo, L., Horvath, A., Moroney, C., Muller, J. P., Paradise, S.  
597 R., Wenkert, D. and Zong, J.: Level 2 Cloud Detection and Classification Algorithm Theoretical  
598 Basis, *Jet Propuls. Lab. Calif. Inst. Technol.*, D-11399(Rev. D), 1999b.

599 Diner, D. J., Abdou, W. A., Ackerman, T. P., Crean, K., Gordon, H. R., Kahn, R. A.,  
600 Martonchik, J. V, McMuldroy, S., Paradise, S. R. and Pinty, B.: Level 2 aerosol retrieval  
601 algorithm theoretical basis, *Jet Propuls. Lab. Calif. Inst. Technol.*, D-11400(Rev. G), 2008.

602 Frankenberg, C., Hasekamp, O., O'Dell, C., Sanghavi, S., Butz, A. and Worden, J.: Aerosol  
603 information content analysis of multi-angle high spectral resolution measurements and its benefit  
604 for high accuracy greenhouse gas retrievals, *Atmos. Meas. Tech.*, 5(7), 1809–1821,  
605 doi:10.5194/amt-5-1809-2012, 2012.



606 Frouin, R. J., Franz, B. A., Ibrahim, A., Knobelspiesse, K., Ahmad, Z., Cairns, B., Chowdhary,  
607 J., Dierssen, H. M., Tan, J., Dubovik, O., Huang, X., Davis, A. B., Kalashnikova, O., Thompson,  
608 D. R., Remer, L. A., Boss, E., Coddington, O., Deschamps, P. Y., Gao, B. C., Gross, L.,  
609 Hasekamp, O., Omar, A., Pelletier, B., Ramon, D., Steinmetz, F. and Zhai, P. W.: Atmospheric  
610 Correction of Satellite Ocean-Color Imagery During the PACE Era, *Front. Earth Sci.*, 7,  
611 doi:10.3389/feart.2019.00145, 2019.

612 Fu, G., Prata, F., Xiang Lin, H., Heemink, A., Segers, A. and Lu, S.: Data assimilation for  
613 volcanic ash plumes using a satellite observational operator: A case study on the 2010  
614 Eyjafjallajökull volcanic eruption, *Atmos. Chem. Phys.*, 17(2), 1187–1205, doi:10.5194/acp-17-  
615 1187-2017, 2017.

616 Gao, B. C., Goetz, A. F. H. and Wiscombe, W. J.: Cirrus cloud detection from Airborne Imaging  
617 Spectrometer data using the 1.38  $\mu\text{m}$  water vapor band, *Geophys. Res. Lett.*, 20(3), 301–304,  
618 doi:10.1029/93GL00106, 1993.

619 Garay, M. J., Witek, M. L., Kahn, R. A., Seidel, F. C., Limbacher, J. A., Bull, M. A., Diner, D.  
620 J., Hansen, E. G. E. G., Kalashnikova, O. V., Lee, H., Nastan, A. M. and Yu, Y.: Introducing the  
621 4.4km spatial resolution Multi-Angle Imaging SpectroRadiometer (MISR) aerosol product,  
622 *Atmos. Meas. Tech.*, 13(2), 593–628, doi:10.5194/amt-13-593-2020, 2020.

623 Gelaro, R., McCarty, W., Suárez, M. J., Todling, R., Molod, A., Takacs, L., Randles, C. A.,  
624 Darmenov, A., Bosilovich, M. G., Reichle, R., Wargan, K., Coy, L., Cullather, R., Draper, C.,  
625 Akella, S., Buchard, V., Conaty, A., da Silva, A. M., Gu, W., Kim, G. K., Koster, R., Lucchesi,  
626 R., Merkova, D., Nielsen, J. E., Partyka, G., Pawson, S., Putman, W., Rienecker, M., Schubert,  
627 S. D., Sienkiewicz, M. and Zhao, B.: The modern-era retrospective analysis for research and  
628 applications, version 2 (MERRA-2), *J. Clim.*, 30(14), 5419–5454, doi:10.1175/JCLI-D-16-  
629 0758.1, 2017.

630 Girolamo, L. Di and Davies, R.: A Band-Differenced Angular Signature Technique for Cirrus  
631 Cloud Detection, *IEEE Trans. Geosci. Remote Sens.*, 32(4), 890–896, doi:10.1109/36.298017,  
632 1994.

633 Girolamo, L. Di and Davies, R.: The Image Navigation Cloud Mask for the Multiangle Imaging

634 Spectroradiometer (MISR), *J. Atmos. Ocean. Technol.*, 12(6), doi:10.1175/1520-  
635 0426(1995)012<1215:tincmf>2.0.co;2, 1995.

636 Gordon, R.: Atmospheric correction of ocean color imagery in the Earth Observing System era,  
637 *J. Geophys. Res. - Atmos.*, 102(D14), 17081–17106, doi:10.1029/96JD02443, 1997.

638 Houweling, S., Hartmann, W., Aben, I., Schrijver, H., Skidmore, J., Roelofs, G. J. and Breon, F.  
639 M.: Evidence of systematic errors in SCIAMACHY-observed CO<sub>2</sub> due to aerosols, *Atmos.*  
640 *Chem. Phys.*, 5(11), 3003–3013, doi:10.5194/acp-5-3003-2005, 2005.

641 Inness, A., Baier, F., Benedetti, A., Bouarar, I., Chabrillat, S., Clark, H., Clerbaux, C., Coheur,  
642 P., Engelen, R. J., Errera, Q., Flemming, J., George, M., Granier, C., Hadji-Lazaro, J., Huijnen,  
643 V., Hurtmans, D., Jones, L., Kaiser, J. W., Kapsomenakis, J., Lefever, K., Leitão, J., Razinger,  
644 M., Richter, A., Schultz, M. G., Simmons, A. J., Suttie, M., Stein, O., Thépaut, J. N., Thouret,  
645 V., Vrekoussis, M. and Zerefos, C.: The MACC reanalysis: An 8 yr data set of atmospheric  
646 composition, *Atmos. Chem. Phys.*, 13(8), 4073–4109, doi:10.5194/acp-13-4073-2013, 2013.

647 Inness, A., Ades, M., Agustí-Panareda, A., Barré, J., Benedictow, A., Blechschmidt, A.-M.,  
648 Dominguez, J. J., Engelen, R., Eskes, H., Flemming, J., Huijnen, V., Jones, L., Kipling, Z.,  
649 Massart, S., Parrington, M., Peuch, V.-H., Razinger, M., Remy, S., Schulz, M. and Suttie, M.:  
650 The CAMS reanalysis of atmospheric composition, *Atmos. Chem. Phys.*, 19(6), 3515–3556,  
651 doi:10.5194/acp-19-3515-2019, 2019.

652 IPCC: Climate Change 2013: The Physical Science Basis. Contribution of Working Group I to  
653 the Fifth Assessment Report of the Intergovernmental Panel on Climate Change, edited by T. F.  
654 Stocker, D. Qin, G. K. Plattner, M. M. B. Tignor, S. K. Allen, J. Boschung, A. Nauels, Y. Xia,  
655 V. Bex, and P. M. Midgley, Cambridge University Press, Cambridge, United Kingdom and New  
656 York, NY, USA., 2013.

657 Kahn, R. A. and Gaitley, B. J.: An analysis of global aerosol type as retrieved by MISR, *J.*  
658 *Geophys. Res. Atmos.*, 120(9), 4248–4281, doi:10.1002/2015JD023322, 2015.

659 Kahn, R. A., Gaitley, B. J., Garay, M. J., Diner, D. J., Eck, T. F., Smirnov, A. and Holben, B. N.:  
660 Multiangle Imaging SpectroRadiometer global aerosol product assessment by comparison with

661 the Aerosol Robotic Network, *J. Geophys. Res. Atmos.*, 115(23), doi:10.1029/2010JD014601,  
662 2010.

663 Kalashnikova, O. V., Garay, M. J., Martonchik, J. V. and Diner, D. J.: MISR Dark Water aerosol  
664 retrievals: Operational algorithm sensitivity to particle non-sphericity, *Atmos. Meas. Tech.*, 6(8),  
665 2131–2154, doi:10.5194/amt-6-2131-2013, 2013.

666 Lamarque, J. F., Shindell, D. T., Josse, B., Young, P. J., Cionni, I., Eyring, V., Bergmann, D.,  
667 Cameron-Smith, P., Collins, W. J., Doherty, R., Dalsoren, S., Faluvegi, G., Folberth, G., Ghan,  
668 S. J., Horowitz, L. W., Lee, Y. H., MacKenzie, I. A., Nagashima, T., Naik, V., Plummer, D.,  
669 Righi, M., Rumbold, S. T., Schulz, M., Skeie, R. B., Stevenson, D. S., Strode, S., Sudo, K.,  
670 Szopa, S., Voulgarakis, A. and Zeng, G.: The atmospheric chemistry and climate model  
671 intercomparison Project (ACCMIP): Overview and description of models, simulations and  
672 climate diagnostics, *Geosci. Model Dev.*, 6(1), 179–206, doi:10.5194/gmd-6-179-2013, 2013.

673 Lelieveld, J., Evans, J. S., Fnais, M., Giannadaki, D. and Pozzer, A.: The contribution of outdoor  
674 air pollution sources to premature mortality on a global scale, *Nature*, 525(7569), 367–371,  
675 doi:10.1038/nature15371, 2015.

676 Levy, R. C., Mattoo, S., Munchak, L. A., Remer, L. A., Sayer, A. M., Patadia, F. and Hsu, N. C.:  
677 The Collection 6 MODIS aerosol products over land and ocean, *Atmos. Meas. Tech.*, 6(11),  
678 2989–3034, doi:10.5194/amt-6-2989-2013, 2013.

679 Liu, M., Westphal, D. L., Walker, A. L., Holt, T. R., Richardson, K. A. and Miller, S. D.:  
680 COAMPS real-time dust storm forecasting during operation Iraqi freedom, *Weather Forecast.*,  
681 22(1), 192–206, doi:10.1175/WAF971.1, 2007.

682 Lynch, P., Reid, J. S., Westphal, D. L., Zhang, J., Hogan, T. F., Hyer, E. J., Curtis, C. A., Hegg,  
683 D. A., Shi, Y., Campbell, J. R., Rubin, J. I., Sessions, W. R., Turk, F. J. and Walker, A. L.: An  
684 11-year global gridded aerosol optical thickness reanalysis (v1.0) for atmospheric and climate  
685 sciences, *Geosci. Model Dev.*, 9(4), 1489–1522, doi:10.5194/gmd-9-1489-2016, 2016.

686 Martonchik, J. V., Diner, D. J., Crean, K. A. and Bull, M. A.: Regional aerosol retrieval results  
687 from MISR, *IEEE Trans. Geosci. Remote Sens.*, 40(7), 1520–1531,

688 doi:10.1109/TGRS.2002.801142, 2002.

689 Martonchik, J. V., Kahn, R. A. and Diner, D. J.: Retrieval of aerosol properties over land using  
690 MISR observations, in *Satellite Aerosol Remote Sensing over Land*, pp. 267–293, Springer  
691 Berlin Heidelberg., 2009.

692 Randles, C. A., da Silva, A. M., Buchard, V., Colarco, P. R., Darmenov, A., Govindaraju, R.,  
693 Smirnov, A., Holben, B., Ferrare, R., Hair, J., Shinozuka, Y. and Flynn, C. J.: The MERRA-2  
694 aerosol reanalysis, 1980 onward. Part I: System description and data assimilation evaluation, *J.*  
695 *Clim.*, 30(17), 6823–6850, doi:10.1175/JCLI-D-16-0609.1, 2017.

696 Reid, J. S., Benedetti, A., Colarco, P. R. and Hansen, J. A.: International operational aerosol  
697 observability workshop, in *Bulletin of the American Meteorological Society*, vol. 92., 2011.

698 Rienecker, M. M., Suarez, M. J., Gelaro, R., Todling, R., Bacmeister, J., Liu, E., Bosilovich, M.  
699 G., Schubert, S. D., Takacs, L., Kim, G. K., Bloom, S., Chen, J., Collins, D., Conaty, A., Da  
700 Silva, A., Gu, W., Joiner, J., Koster, R. D., Lucchesi, R., Molod, A., Owens, T., Pawson, S.,  
701 Pegion, P., Redder, C. R., Reichle, R., Robertson, F. R., Ruddick, A. G., Sienkiewicz, M. and  
702 Woollen, J.: MERRA: NASA’s modern-era retrospective analysis for research and applications,  
703 *J. Clim.*, 24, 3624–3648, doi:10.1175/JCLI-D-11-00015.1, 2011.

704 Sayer, A. M. and Knobelspiesse, K. D.: How should we aggregate data? Methods accounting for  
705 the numerical distributions, with an assessment of aerosol optical depth, *Atmos. Chem. Phys.*,  
706 19(23), 15023–15048, doi:10.5194/acp-19-15023-2019, 2019.

707 Sayer, A. M., Govaerts, Y., Kolmonen, P., Lipponen, A., Luffarelli, M., Mielonen, T., Patadia,  
708 F., Popp, T., Povey, A. C., Stebel, K. and Witek, M. L.: A review and framework for the  
709 evaluation of pixel-level uncertainty estimates in satellite aerosol remote sensing, *Atmos. Meas.*  
710 *Tech.*, 13(2), 373–404, doi:10.5194/amt-13-373-2020, 2020.

711 Sekiyama, T. T., Tanaka, T. Y., Shimizu, A. and Miyoshi, T.: Data assimilation of CALIPSO  
712 aerosol observations, *Atmos. Chem. Phys.*, 10(1), 39–49, doi:10.5194/acp-10-39-2010, 2010.

713 Shi, Y., Zhang, J., Reid, J. S., Holben, B., Hyer, E. J. and Curtis, C.: An analysis of the collection  
714 5 MODIS over-ocean aerosol optical depth product for its implication in aerosol assimilation,

715 Atmos. Chem. Phys., 11(2), 557–565, doi:10.5194/acp-11-557-2011, 2011.

716 Shi, Y., Zhang, J., Reid, J. S., Hyer, E. J. and Hsu, N. C.: Critical evaluation of the MODIS Deep  
717 Blue aerosol optical depth product for data assimilation over North Africa, Atmos. Meas. Tech.,  
718 6(4), 949–969, doi:10.5194/amt-6-949-2013, 2013.

719 Shi, Y., Zhang, J., Reid, J. S., Liu, B. and Hyer, E. J.: Critical evaluation of cloud contamination  
720 in the MISR aerosol products using MODIS cloud mask products, Atmos. Meas. Tech., 7(6),  
721 1791–1801, doi:10.5194/amt-7-1791-2014, 2014.

722 Shindell, D. T., Lamarque, J. F., Schulz, M., Flanner, M., Jiao, C., Chin, M., Young, P. J., Lee,  
723 Y. H., Rotstajn, L., Mahowald, N., Milly, G., Faluvegi, G., Balkanski, Y., Collins, W. J.,  
724 Conley, A. J., Dalsoren, S., Easter, R., Ghan, S., Horowitz, L., Liu, X., Myhre, G., Nagashima,  
725 T., Naik, V., Rumbold, S. T., Skeie, R., Sudo, K., Szopa, S., Takemura, T., Voulgarakis, A.,  
726 Yoon, J. H. and Lo, F.: Radiative forcing in the ACCMIP historical and future climate  
727 simulations, Atmos. Chem. Phys., 13(6), 2939–2974, doi:10.5194/acp-13-2939-2013, 2013.

728 Si, Y., Chen, L., Xiong, X., Shi, S., Husi, L. and Cai, K.: Evaluation of the MISR fine resolution  
729 aerosol product using MODIS, MISR, and ground observations over China, Atmos. Environ.,  
730 223(December 2019), 117229, doi:10.1016/j.atmosenv.2019.117229, 2020.

731 Sogacheva, L., Popp, T., Sayer, A. M., Dubovik, O., Garay, M. J., Heckel, A., Hsu, N. C.,  
732 Jethva, H., Kahn, R. A., Kolmonen, P., Kosmale, M., de Leeuw, G., Levy, R. C., Litvinov, P.,  
733 Lyapustin, A., North, P., Torres, O. and Arola, A.: Merging regional and global aerosol optical  
734 depth records from major available satellite products, Atmos. Chem. Phys., 20(4), 2031–2056,  
735 doi:10.5194/acp-20-2031-2020, 2020.

736 Tao, M., Wang, J., Li, R., Chen, L., Xu, X., Wang, L., Tao, J., Wang, Z. and Xiang, J.:  
737 Characterization of Aerosol Type Over East Asia by 4.4 km MISR Product: First Insight and  
738 General Performance, J. Geophys. Res. Atmos., 125(13), 1–16, doi:10.1029/2019JD031909,  
739 2020.

740 Di Tomaso, E., Schutgens, N. A. J., Jorba, O. and García-Pando, C. P.: Assimilation of MODIS  
741 Dark Target and Deep Blue observations in the dust aerosol component of NMMB-MONARCH

742 version 1.0, *Geosci. Model Dev.*, 10(3), 1107–1129, doi:10.5194/gmd-10-1107-2017, 2017.

743 Turnock, S. T., Allen, R. J., Andrews, M., Bauer, S. E., Deushi, M., Emmons, L., Good, P.,  
744 Horowitz, L., John, J. G., Michou, M., Nabat, P., Naik, V., Neubauer, D., O'Connor, F. M.,  
745 Olivié, D., Oshima, N., Schulz, M., Sellar, A., Shim, S., Takemura, T., Tilmes, S., Tsigaridis, K.,  
746 Wu, T. and Zhang, J.: Historical and future changes in air pollutants from CMIP6 models,  
747 *Atmos. Chem. Phys.*, 20(23), 14547–14579, doi:10.5194/acp-20-14547-2020, 2020.

748 Werner, M., Kryza, M. and Guzikowski, J.: Can data assimilation of surface PM<sub>2.5</sub> and Satellite  
749 AOD improve WRF-Chem Forecasting? A case study for two scenarios of particulate air  
750 pollution episodes in Poland, *Remote Sens.*, 11(20), doi:10.3390/rs11202364, 2019.

751 Witek, M. L., Garay, M. J., Diner, D. J. and Smirnov, A.: Aerosol optical depths over oceans: A  
752 view from MISR retrievals and collocated MAN and AERONET in situ observations, *J.*  
753 *Geophys. Res. Atmos.*, 118(22), 12620–12633, doi:10.1002/2013JD020393, 2013.

754 Witek, M. L., Diner, D. J., Garay, M. J., Xu, F., Bull, M. A. and Seidel, F. C.: Improving MISR  
755 AOD Retrievals with Low-Light-Level Corrections for Veiling Light, *IEEE Trans. Geosci.*  
756 *Remote Sens.*, 56(3), 1251–1268, doi:10.1109/TGRS.2017.2727342, 2018a.

757 Witek, M. L., Garay, M. J., Diner, D. J., Bull, M. A. and Seidel, F. C.: New approach to the  
758 retrieval of AOD and its uncertainty from MISR observations over dark water, *Atmos. Meas.*  
759 *Tech.*, 11(1), 429–439, doi:10.5194/amt-11-429-2018, 2018b.

760 Witek, M. L., Garay, M. J., Diner, D. J. and Smirnov, A.: Oceanic Aerosol Loading Derived  
761 From MISR's 4.4 km (V23) Aerosol Product, *J. Geophys. Res. Atmos.*, 124(17–18), 10154–  
762 10174, doi:10.1029/2019JD031065, 2019.

763 Xian, P., Reid, J. S., Hyer, E. J., Sampson, C. R., Rubin, J. I., Ades, M., Asencio, N., Basart, S.,  
764 Benedetti, A., Bhattacharjee, P. S., Brooks, M. E., Colarco, P. R., da Silva, A. M., Eck, T. F.,  
765 Guth, J., Jorba, O., Kouznetsov, R., Kipling, Z., Sofiev, M., Perez Garcia-Pando, C., Pradhan,  
766 Y., Tanaka, T., Wang, J., Westphal, D. L., Yumimoto, K. and Zhang, J.: Current state of the  
767 global operational aerosol multi-model ensemble: An update from the International Cooperative  
768 for Aerosol Prediction (ICAP), *Q. J. R. Meteorol. Soc.*, 145, 176–209, doi:10.1002/qj.3497,

769 2019.

770 Zhang, J. and Reid, J. S.: An analysis of clear sky and contextual biases using an operational  
771 over ocean MODIS aerosol product, *Geophys. Res. Lett.*, 36(15), doi:10.1029/2009GL038723,  
772 2009.

773 Zhang, J. and Reid, J. S.: A decadal regional and global trend analysis of the aerosol optical  
774 depth using a data-assimilation grade over-water MODIS and Level 2 MISR aerosol products,  
775 *Atmos. Chem. Phys.*, 10(22), 10949–10963, doi:10.5194/acp-10-10949-2010, 2010.

776 Zhang, J., Reid, J. S., Westphal, D. L., Baker, N. L. and Hyer, E. J.: A system for operational  
777 aerosol optical depth data assimilation over global oceans, *J. Geophys. Res. Atmos.*, 113(10), 1–  
778 13, doi:10.1029/2007JD009065, 2008.

779